

## Co on Fe<sub>3</sub>O<sub>4</sub>(001): Towards precise control of surface properties

Raquel Gargallo-Caballero, Laura Martín-García, Adrián Quesada, Cecilia Granados-Miralles, Michael Foerster, Lucía Aballe, Roland Bliem, Gareth S. Parkinson, Peter Blaha, José F. Marco, and Juan de la Figuera

Citation: *The Journal of Chemical Physics* **144**, 094704 (2016); doi: 10.1063/1.4942662

View online: <http://dx.doi.org/10.1063/1.4942662>

View Table of Contents: <http://scitation.aip.org/content/aip/journal/jcp/144/9?ver=pdfcov>

Published by the AIP Publishing

---

### Articles you may be interested in

On the electronic, structural, and thermodynamic properties of Au supported on  $\alpha$ -Fe<sub>2</sub>O<sub>3</sub> surfaces and their interaction with CO

*J. Chem. Phys.* **143**, 034704 (2015); 10.1063/1.4926835

Vacancy dependent structural, electronic, and magnetic properties of zigzag silicene nanoribbons:Co

*J. Appl. Phys.* **114**, 163711 (2013); 10.1063/1.4828482

Fe<sub>3</sub>O<sub>4</sub> films on Ag(001)—Generation of high-quality epitaxial ferrimagnetic metal oxide films

*Appl. Phys. Lett.* **103**, 052401 (2013); 10.1063/1.4816787

Contaminants Induced Onset of Nanostripes and Nanotrenches on the Fe<sub>3</sub>O<sub>4</sub> (001) Surface

*AIP Conf. Proc.* **696**, 879 (2003); 10.1063/1.1639797

Charge Ordering on the  $(\sqrt{2} \times \sqrt{2})R45^\circ$  Reconstructed Fe<sub>3</sub>O<sub>4</sub> (001) Surface

*AIP Conf. Proc.* **696**, 873 (2003); 10.1063/1.1639796

---

The cover of the AIP Applied Physics Reviews journal. It features a blue and orange color scheme with a molecular structure background. The title 'AIP Applied Physics Reviews' is at the top, and a diagram of a device structure is in the center.

## NEW Special Topic Sections

**NOW ONLINE**  
Lithium Niobate Properties and Applications:  
Reviews of Emerging Trends

**AIP** Applied Physics Reviews

# Co on Fe<sub>3</sub>O<sub>4</sub>(001): Towards precise control of surface properties

Raquel Gargallo-Caballero,<sup>1</sup> Laura Martín-García,<sup>1</sup> Adrián Quesada,<sup>2</sup>  
Cecilia Granados-Miralles,<sup>3</sup> Michael Foerster,<sup>4</sup> Lucía Aballe,<sup>4</sup> Roland Blum,<sup>5</sup>  
Gareth S. Parkinson,<sup>5</sup> Peter Blaha,<sup>6</sup> José F. Marco,<sup>1</sup> and Juan de la Figuera<sup>1,a)</sup>

<sup>1</sup>*Instituto de Química Física "Rocasolano," CSIC, Madrid E-28006, Spain*

<sup>2</sup>*Instituto de Cerámica y Vidrio, CSIC, Madrid E-28049, Spain*

<sup>3</sup>*Department of Chemistry, Aarhus University, Langelandsgade 140, Århus DK-8000, Denmark*

<sup>4</sup>*ALBA Synchrotron, CELLS, Barcelona, E-08290, Spain*

<sup>5</sup>*Institute of Applied Physics, Vienna University of Technology, Vienna A-1040, Austria*

<sup>6</sup>*Institute of Materials Chemistry, Vienna University of Technology, Vienna A-1060, Austria*

(Received 7 December 2015; accepted 12 February 2016; published online 2 March 2016)

A novel approach to incorporate cobalt atoms into a magnetite single crystal is demonstrated by a combination of x-ray spectro-microscopy, low-energy electron diffraction, and density-functional theory calculations. Co is deposited at room temperature on the reconstructed magnetite (001) surface filling first the subsurface octahedral vacancies and then occupying adatom sites on the surface. Progressive annealing treatments at temperatures up to 733 K diffuse the Co atoms into deeper crystal positions, mainly into octahedral ones with a marked inversion level. The oxidation state, coordination, and magnetic moments of the cobalt atoms are followed from their adsorption to their final incorporation into the bulk, mostly as octahedral Co<sup>2+</sup>. This precise control of the near-surface Co atoms location opens up the way to accurately tune the surface physical and magnetic properties of mixed spinel oxides. © 2016 Author(s). All article content, except where otherwise noted, is licensed under a Creative Commons Attribution (CC BY) license (<http://creativecommons.org/licenses/by/4.0/>). [<http://dx.doi.org/10.1063/1.4942662>]

## I. INTRODUCTION

Mesoscopic oxides constitute a fascinating family of materials due to the wide range of functional properties that they offer. The ongoing challenge associated with these systems comes from the ever growing demand of miniaturization and device performance in a variety of applications, which calls for an extremely high level of control over the structural properties at the nanoscale. In this context, the spinel structure, AB<sub>2</sub>O<sub>4</sub>, is an interesting example.<sup>1</sup> It consists of an fcc lattice of oxygen anions, with (metal) cations occupying interstitial tetrahedral (A) and twice as many octahedral (B) sites. The classic spinel structure has the divalent/trivalent cations in the tetrahedral/octahedral sites, respectively. However, an inversion in the cationic distribution is possible, and cations with other oxidation states (for example, 1+ or 4+) can be also accommodated in the spinel structure. This chemical flexibility is the reason for the wide variety of properties that they present, and its control enables to obtain engineered functionalities. A classic example is the family of Co-Fe spinel oxides,<sup>2-4</sup> spanning from the iron-only inverse spinel (Fe<sub>3</sub>O<sub>4</sub>), a presumed half-metal ferrimagnetic conductor with a high Curie temperature of 850 K,<sup>5</sup> to the cobalt-only direct spinel (Co<sub>3</sub>O<sub>4</sub>), an antiferromagnetic insulator.<sup>6</sup> One particular mixed oxide, CoFe<sub>2</sub>O<sub>4</sub>, has the highest magnetocrystalline anisotropy of all iron-containing spinels.<sup>7</sup> The applications of Co-Fe spinel oxides span from permanent magnets,<sup>8</sup> and

spintronic devices,<sup>9-13</sup> through catalysis<sup>14-19</sup> to electrochemistry where they are proposed as high-performance anodes in Li-batteries.<sup>20-22</sup>

The catalytic properties of specific oxides stem partially from the particular arrangement of Fe and Co cations at the surface under the given operation conditions. Furthermore the surfaces can present additional cation arrangements not available in the bulk. For example, it has been suggested that octahedral Co<sup>2+</sup> is the active site for H<sub>2</sub>O<sub>2</sub> decomposition<sup>23</sup> or that the replacement of Co<sup>3+</sup> by Fe<sup>3+</sup> leads to a partial loss of activity towards CO oxidation.<sup>24</sup> Changing the detailed cation arrangement at the near surface region also crucially alters the magnetic properties,<sup>25</sup> with an impact in the use of iron-cobalt oxides in spin-valve devices.<sup>26</sup> It is thus crucial to be able to determine the oxidation state and locate the cations in the near surface region in such mixed oxides.

Thus, we present here a novel approach for obtaining ultrathin cobalt ferrite films on Fe<sub>3</sub>O<sub>4</sub>(001) crystals that consists in depositing Co atoms on the ( $\sqrt{2} \times \sqrt{2}$ )R45° reconstruction,<sup>27</sup> followed by annealing steps. In order to follow the evolution of the properties as the cobalt atoms are incorporated into the magnetite structure, we combine low-energy electron diffraction (LEED), density functional theory (DFT) calculations, x-ray absorption (XAS) and x-ray magnetic circular dichroism (XMCD) in photoemission electron microscopy (PEEM). This approach enables controlling the particular location and oxidation state of the Co cations at the surface by adjusting the Co dose and the annealing procedure. Moreover, the evaluation of the magnetic moments of the specific cations is brought forward

a) [juan.delafiguera@iqfr.csic.es](mailto:juan.delafiguera@iqfr.csic.es)

as a powerful tool for determining the chemical environment at the ultrathin limit.

## II. EXPERIMENTAL METHODS

The experiments were performed on a natural magnetite crystal from Mali whose surface was prepared by repeated Ar<sup>+</sup> sputtering at 1–1.5 kV and annealing cycles of up to 870 K in a background oxygen pressure of 10<sup>−6</sup> mbar. After preparation, the surface presented the ( $\sqrt{2} \times \sqrt{2}$ )R45° reconstruction.

Cobalt was dosed from a cobalt rod heated by electron bombardment with a water-cooled heat shield. The doser was calibrated by growth on Ru(0001), where 1 ML corresponds to a complete layer with the same density as the Ru surface. The doses are described both in ML and in terms of the number of atoms deposited per area of the unit cell of the ( $\sqrt{2} \times \sqrt{2}$ )R45° reconstructed surface (atoms per unit cell (u.c.) or at/u.c.). The latter corresponds to a density of  $1.42 \times 10^{14}$  cm<sup>−2</sup>. The rate employed is  $6 \times 10^{-3}$  at u.c.<sup>−1</sup> s<sup>−1</sup>. After deposition, progressive annealing steps were performed followed by cooling down to room temperature for the spectroscopic measurements. The sample temperature was measured by a WRe thermocouple welded to the support washer underneath the sample.

The surface of the sample was characterized *in situ* by a combined low-energy electron and photoelectron microscope at the CIRCE beamline of the ALBA Synchrotron.<sup>28</sup> In pure low-energy electron microscopy (LEEM)<sup>29</sup> mode, the microscope is used for microspot low-energy diffraction measurements and real-time imaging in bright or dark-field LEEM. It can be used in photoelectron microscopy mode (XPEEM), i.e., with x-rays, where images are acquired with the energy-filtered photoelectrons from micron-sized selected areas of the surface with an energy resolution down to 0.2 eV. The x-ray beam impinges on the sample at an angle of 16° from the surface plane, and the azimuth of the sample can be modified at will. The kinetic energy of the photoelectrons used to form the image can also be selected.

The XAS and XMCD spectra were obtained in remanence from sequences of PEEM images acquired at different photon energies scanning the Fe and Co *L* absorption edges (700–760 eV and 770–805 eV for Fe and Co, respectively) with circularly polarized x-rays of both helicities, positive ( $\mu+$ ) and negative ( $\mu-$ ). The images were recorded collecting the secondary electrons with a kinetic energy of 2 eV, equivalent to the total electron yield mode. The particular energies for the shown XMCD images correspond to the main peak for the Co XMCD spectra and the first minimum of the Fe XMCD spectra. To obtain the XMCD difference, the x-ray absorption spectra on neighboring magnetic domains with opposite magnetization were used. In order to remove nonmagnetic contributions, spectra from each domain with a given light helicity were averaged with the spectra from the opposite domain measured with the opposite light helicity.<sup>30,31</sup> The element specific spin and orbital magnetic moments ( $m_{\text{orb}}$  and  $m_{\text{spin}}$ , respectively) per cation were estimated from the application of the so-called sum rules<sup>32</sup> after subtraction of an hyperbolic-like background. In order to obtain the spin and

orbital magnetic moments per cation applying the sum rules, the number of *d* holes in each cation should be known. For the sake of simplicity, we have assumed a constant oxidation state for each cation for the magnetic moment determination: we assume Fe to be in the Fe<sup>3+</sup> state and Co in the Co<sup>2+</sup> state. This introduces an additional error of ( $\approx 15\%$ ) for the former and none for the latter. The same applies to the self-absorption corrections, which have been omitted. They should not be necessary for Co, and for Fe, they would give a constant contribution that does not change trends in the experimental data.

## III. DENSITY FUNCTIONAL THEORY CALCULATIONS

The DFT calculations were performed using the full-potential augmented plane wave + local orbital (APW+lo) method as implemented in WIEN2k.<sup>33</sup> We use the generalized gradient approximation of Perdew *et al.*<sup>34</sup> with a Hubbard potential *U* (*U*<sub>eff</sub> = 3.8 eV) to treat the highly correlated Fe and Co 3*d* electrons. The surface was modeled by a  $\sqrt{2} \times \sqrt{2}$  supercell of B-layer terminated Fe<sub>3</sub>O<sub>4</sub> with 17 Fe-layers and a vacuum layer of >12.5 Å separating the periodic slabs. The cells include a total of 124 atoms. The total energies were calculated with lattice parameters of bulk magnetite optimized for *U*<sub>eff</sub> = 3.8 eV. In a reference calculation performed with *U*<sub>eff,Co</sub> = 0 eV for Co incorporated in a subsurface octahedral site, no significant difference was observed. Atomic sphere sizes of 0.98, 0.79, and 1.0 Å were used for Fe, O, and Co, respectively. The energies of the studied configurations were compared to the sum of the total energies of two free Co atoms in an otherwise empty cell and a pristine magnetite slab. A plane-wave cutoff of  $RK_{\text{max}} = 7.0$  corresponding to 296.6 eV was used, and the Brillouin zones of the surface models were sampled with a  $3 \times 3 \times 1$  k-mesh. The surface models were relaxed until all forces were below 1 mRy/bohr (26 meV/Å). A Fermi broadening of 0.08 eV was employed.

## IV. RESULTS

### A. Experimental observations

After cleaning, the magnetite surface presents the well-known ( $\sqrt{2} \times \sqrt{2}$ )R45° reconstruction.<sup>27</sup> LEED patterns of the surface were acquired during deposition of  $\approx 6$  Co at/u.c. (0.5 ML) at room temperature, with selected frames shown in Figure 1. The reconstruction spots disappeared completely after deposition of 1–2 Co at/u.c. No further changes were detected in the LEED pattern during the deposition of the additional 5 at/u.c.

The XMCD-PEEM image measured at the Fe *L*-edge (in particular, at 707 eV photon energy) is shown in Figure 2(a). Magnetite (001) displays a complex multiscale magnetic domains pattern,<sup>35,36</sup> with arrays of lines and curved domains. The origin of such complex micromagnetic structure is the competition between the shape anisotropy and the magnetocrystalline anisotropy. As a result, the  $\langle 111 \rangle$  bulk easy axes turn in the surface region into the  $[110]$  and  $[1\bar{1}0]$  ones. The sample was aligned so the  $[110]$  axis lies along the in-plane component of the x-ray incoming direction.

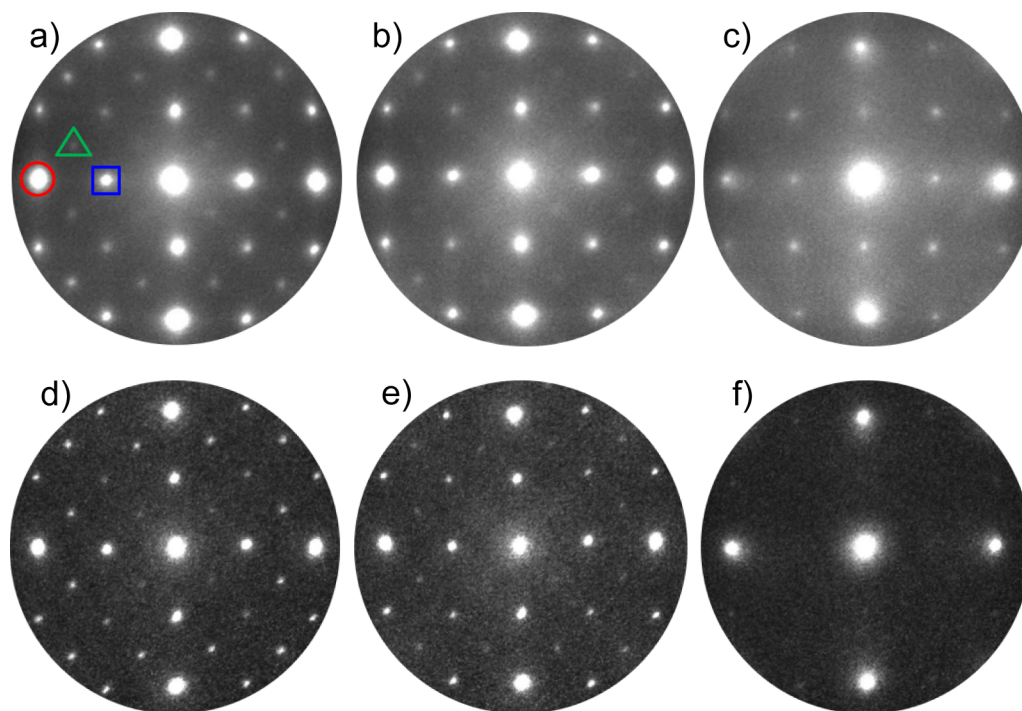


FIG. 1. LEED patterns acquired during Co deposition on magnetite (001). During deposition of a dose of 6 Co at/u.c.: (a) 0 at/u.c., (b) 1 at/u.c., and (c) 6 at/u.c. During deposition of a dose of 25 at/u.c.: (d) 0 at/u.c., (e) 1 at/u.c., and (f) 8 at/u.c. The spots marked on (a) correspond to a first order beam (blue square), a reconstruction beam (green triangle), and a second order beam (red circle). The electron energy is 40 eV.

As in XMCD the observed contrast is for domains with magnetization along the x-ray direction, in Figure 2(a) we observe the domains along the  $[110]$  axis. The gray areas correspond to domains that have no component along the  $[110]$  direction, i.e., domains with the magnetization mostly along the  $[1\bar{1}0]$  direction. The surface domains after deposition of 6 Co at/u.c. exactly match those of the clean magnetite surface.

Figure 2(c) displays the Fe  $L$ -edge XAS and XMCD spectra of the magnetite surface after room temperature deposition of 6 Co at/u.c. The Fe XMCD spectrum has a prominent three peak structure at each absorption edge. In particular, at the Fe  $L_3$  edge, two downward peaks surround an upward peak. These are usually interpreted as arising from octahedral  $\text{Fe}^{2+}$  (low-energy downward peak), tetrahedral  $\text{Fe}^{3+}$  (central upward peak), and octahedral  $\text{Fe}^{3+}$

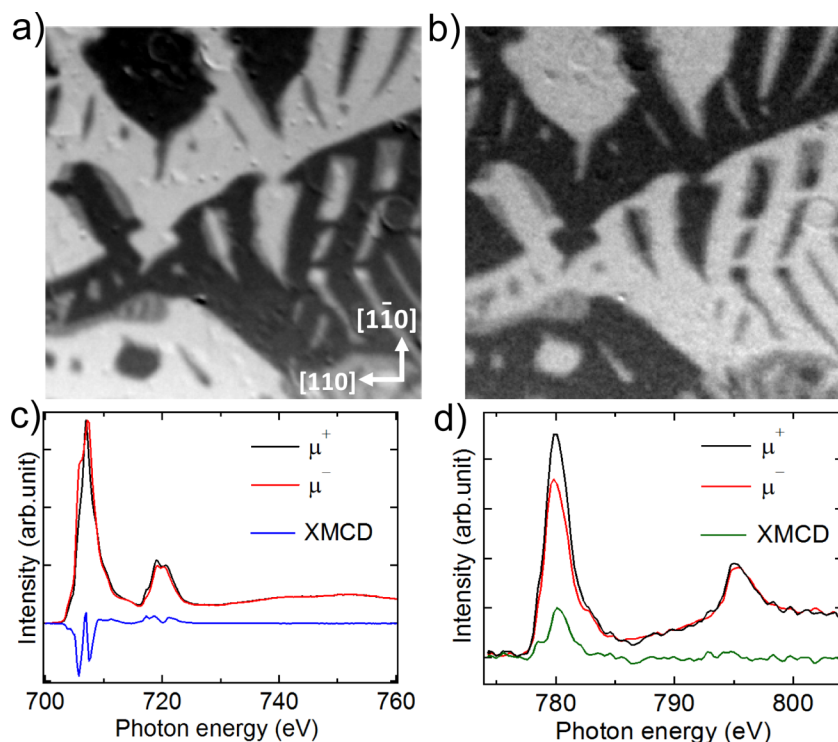


FIG. 2. XMCD characterization of the magnetite surface after room temperature deposition of 6 Co at/u.c. The XMCD images are  $18\ \mu\text{m}$  wide. (a) XMCD-PEEM image measured at the Fe  $L$ -edge. (b) XMCD-PEEM image measured at the Co  $L$ -edge. (c) Fe  $L$ -edge XAS and XMCD spectra. (d) Co  $L$ -edge XAS and XMCD spectra.  $\mu^+$  and  $\mu^-$  refer to XAS spectra acquired with positive and negative helicities, respectively.



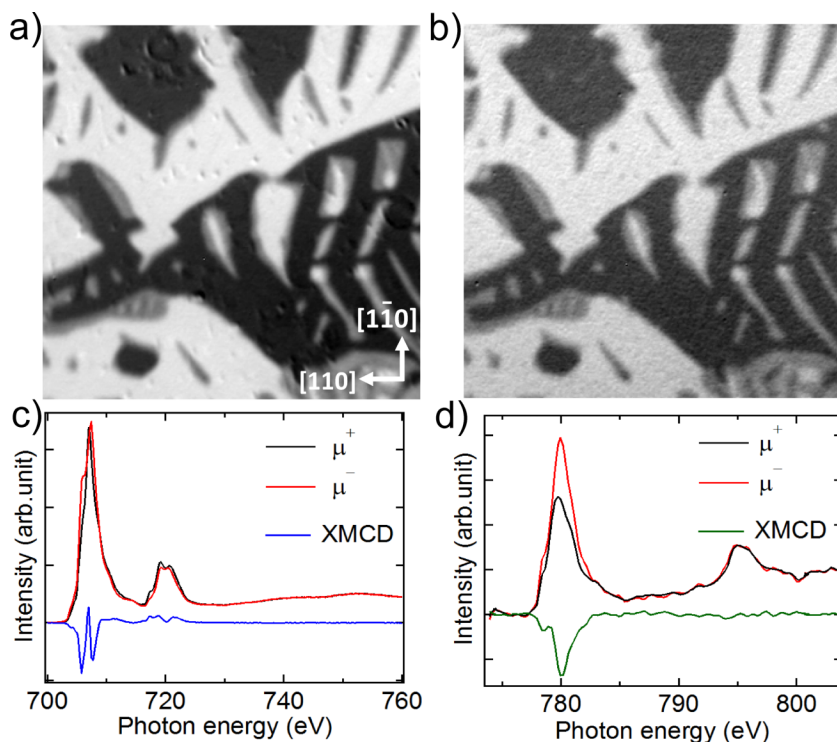


FIG. 3. XMCD characterization of the Co/Fe<sub>3</sub>O<sub>4</sub> surface after deposition of 6 Co at/u.c. and annealing to 553 K. The XMCD images are 18  $\mu\text{m}$  wide. (a) XMCD-PEEM image measured at the Fe  $L$ -edge. (b) XMCD-PEEM image measured at the Co  $L$ -edge. (c) Fe  $L$ -edge XAS and XMCD spectra. (d) Co  $L$ -edge XAS and XMCD spectra.  $\mu^+$  and  $\mu^-$  refer to XAS spectra acquired with positive and negative helicities, respectively.

(high-energy downward peak), respectively. We caution that this is a simplistic interpretation<sup>37</sup> which is problematic for an accurate determination (as full multiplet calculations show that, for example, part of the initial peak corresponds to octahedral Fe<sup>3+</sup>), but it can serve as a guide of the magnetic orientation of each cation: the iron cations in the octahedral positions are ferromagnetically coupled between them and antiferromagnetically coupled to those in the tetrahedral ones. Since the XMCD-PEEM image is acquired at the peak energy of the octahedral Fe<sup>2+</sup> contribution, it reflects the magnetization orientation of such cations.

The Co  $L$ -edge XMCD-PEEM images were acquired at the maximum of the  $L_3$  peak. Detailed comparison between the Fe and Co XMCD-PEEM images shows that the domains observed for both cases are exactly the same, sharing the same gray areas. Thus, the magnetic easy axes of the surface are unchanged and correspond to the easy axes of pure magnetite. However, the contrast is reversed: where a black domain is observed in the iron cation image, white is detected in the cobalt one. In other words, the coupling between the Co atoms and the Fe<sub>oct</sub> atoms is antiferromagnetic. In addition, the Co XMCD spectrum has the shape characteristic of Co<sup>2+</sup> cations.<sup>38</sup> Thus, upon depositing 6 Co at/u.c. at room temperature on magnetite (001), Co atoms preferentially become Co<sup>2+</sup> and are antiferromagnetically coupled to Fe<sub>oct</sub>. The estimated magnetic moments are  $m_{\text{spin}} = +0.7 \mu_B$  and  $m_{\text{orb}} = +0.1 \mu_B$  for Fe and  $m_{\text{spin}} = -0.6 \mu_B$  and  $m_{\text{orb}} = -0.2 \mu_B$  for Co, with the sign indicating the orientation relative to the average Fe magnetic moment, which corresponds to that of the Fe<sub>oct</sub> sublattice.

The sample was then annealed to 553 K for 20 min and cooled down back to room temperature in order to promote cation interdiffusion.<sup>39</sup> The resulting Fe and Co XMCD-PEEM

images, together with the  $L$ -edge XAS and XMCD spectra, are shown in Figure 3. The domains have the same shape and distribution as in the previous case, but comparing the Fe and Co XMCD images, it is evident that coupling of the Co and the Fe has changed: now all the black and white domains have the same orientation in both images. Thus, the average Co magnetic moment orientation is now the same as the Fe<sub>oct</sub> atoms, as is evident also by comparing the XMCD spectra (Figure 3). While the Fe spectrum is very similar to the previous one (before annealing), the Co dichroic spectrum is now negative through all the  $L_3$  absorption edge. Nevertheless, its shape is still indicative of a Co<sup>2+</sup> oxidation state. The estimated magnetic moments for Fe are unchanged, whereas for Co they have changed to  $+0.8 \mu_B$  and  $+0.5 \mu_B$  for the spin and orbital components, respectively (Figure 4).

After one hour of annealing treatment of the crystal at 673 K, the Co atoms diffuse deeper into the bulk. The sample

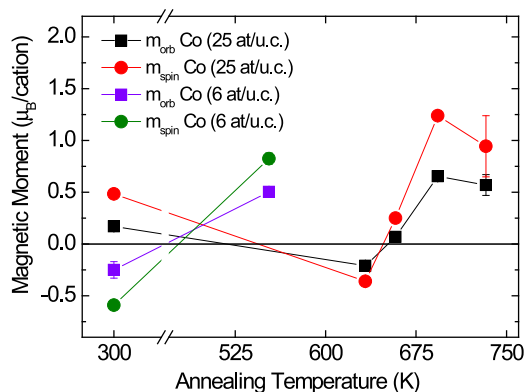


FIG. 4. Average spin and orbital magnetic moments per Co cation vs. the annealing temperature estimated by XMCD sum rules.

surface was then prepared again by repeated  $\text{Ar}^+$  sputtering at 1–1.5 kV and annealing cycles of up to 870 K in a background oxygen pressure of  $10^{-6}$  mbar in order to recover the original reconstructed crystal surface. Then, we perform a second deposition of further 25 Co at/u.c. ( $\approx 2$  ML). Again the  $(\sqrt{2} \times \sqrt{2})\text{R}45^\circ$  surface reconstruction was removed after deposition of 1–2 Co at/u.c. In addition, after the deposition of 8 Co at/u.c., the  $(1 \times 1)$  spots also disappeared (Figure 1). The characteristic profile of the  $\text{Co}^{2+}$  cation dichroic spectrum is again revealed in the Co XMCD spectrum (not shown). Fe and Co domains match once more not only in shape and distribution but also in coupling, i.e., black/white domains in Co are black/white in Fe demonstrating that the average Co magnetic moment is oriented in the same direction as the one from octahedral Fe, i.e., they are ferromagnetically coupled.

The sample was then annealed in four subsequent steps (from 633 to 733 K), cooling down to room temperature after each annealing step in order to perform the XMCD measurements. The first annealing treatment (633 K) was for 10 min and the others for 5 min. In all cases, perfect agreement between the Fe and Co domain distribution was found. However, the coupling changed twice: from the parallel alignment of the Co and Fe in the as-grown configuration to an antiparallel alignment after annealing to 633 K and again to parallel alignment for the final annealing steps. Figure 4 summarizes the obtained spin and orbital magnetic moments at the different stages, displaying the non-monotonic evolution of the Co moments. The initial magnetic moment is  $m_{\text{spin}} = +0.5 \mu_B$  and  $m_{\text{orb}} = +0.2 \mu_B$ , which becomes  $m_{\text{spin}} = -0.4 \mu_B$  and  $m_{\text{orb}} = -0.2 \mu_B$  after annealing at 633 K. Annealing to 658 K gave back positive values for the magnetic moment of  $m_{\text{spin}} = +0.2 \mu_B$  and  $m_{\text{orb}} = +0.1 \mu_B$ . Subsequent annealing treatments lead to an increased magnetic moment of  $m_{\text{spin}} = +1.2 \mu_B$  and  $m_{\text{orb}} = +0.7 \mu_B$ . For the final stage corresponding to the highest annealing temperature, the Co atoms diffuse deeper into the bulk, and thus, the intensity of the XAS measurements decreases strongly, resulting in much larger errors in the estimated magnetic moments. Taking into account this large error, the values can be considered similar to the previous annealing step.

The Co 2*p* core level XPS spectra for the as-deposited surface with 25 at/u.c. and after annealing treatments at 633 K

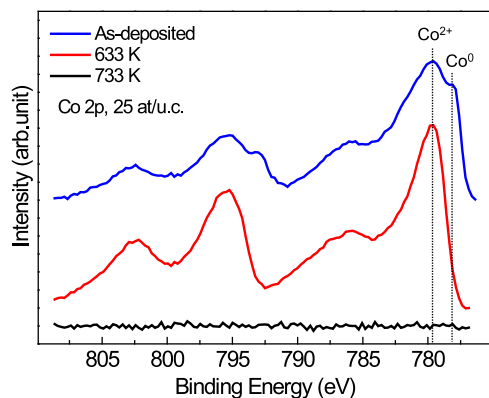


FIG. 5. Co 2*p* XPS core level spectra just after depositing 25 at/u.c. and after subsequent annealing steps.

and 733 K are shown in Figure 5. The spectra corresponding to the annealing temperatures of 658 K and 693 K present no evident changes compared to those after annealing at 633 K and 733 K, respectively (not shown). The spectrum from the as-deposited surface with 25 at/u.c. surface contains two spin-orbit doublets (characterized by their respective Co 2*p*<sub>3/2</sub> binding energies of 778.0 and 779.5 eV) and evident shake-up satellite structure near 786 and 803 eV. The first spin-orbit doublet is associated with metallic Co, while the second, together with the satellite structure, is characteristic of a  $\text{Co}^{2+}$  species. After annealing to 633 K, the metallic Co contribution disappears and only the  $\text{Co}^{2+}$  component remains, which implies that the temperature treatment brings about the incorporation of Co in the crystal lattice as  $\text{Co}^{2+}$ . Attempts to fit these spectra suggest the possible presence of some  $\text{Co}^{3+}$ , which could allow explaining the magnetic moment behavior with the annealing temperature as seen later on.

After the last annealing step to 733 K, no Co is detected by XPS (Figure 5), while it is still observed by XAS/XMCD. The reason for this discrepancy is that the probing depth of the two methods is different, being larger for the XAS measurements. In particular, for XAS measurements performed at low kinetic energies, recent experiments estimate a probing depth of 1.3 nm.<sup>40</sup> Instead, the XPS measurements were performed at a constant x-ray energy of 890 eV, and a kinetic energy from 80 to 115 eV, thus, near the minimum of the universal mean free path curve. The estimated electron attenuation length at these energies is about 0.3 nm as calculated from the NIST database. Thus, we estimate that Co is at least a few nm below the crystal surface after the last annealing step.

## B. DFT results

The adsorption and incorporation of single Co atoms at the  $\text{Fe}_3\text{O}_4(001)$  surface were modelled using density functional theory calculations. The calculations are based on the so-called B-layer termination of this surface, consisting of octahedrally coordinated Fe ( $\text{Fe}_{\text{oct}}$ ) and oxygen atoms. The  $(\sqrt{2} \times \sqrt{2})\text{R}45^\circ$ -reconstructed B-layer is the most stable surface termination<sup>27</sup> under UHV conditions and can be prepared reproducibly in experiments. The surface reconstruction is based on a rearrangement in the cation lattice in the subsurface layers. Specifically, two  $\text{Fe}_{\text{oct}}$  atoms in the second subsurface layer are replaced by one additional tetrahedrally coordinated Fe atom in the first subsurface layer.<sup>27</sup> The  $\text{Fe}_{\text{oct}}$  vacancies and the additional  $\text{Fe}_{\text{tet}}$  are labelled, respectively,  $V_{\text{Fe}}$  and  $\text{Fe}_{\text{int}}$  in Figure 6(a). Thus the surface region is missing one Fe cation compared to bulk  $\text{Fe}_3\text{O}_4$  and can be seen as an oxidized termination. The iron atoms in the first six layers all acquire an  $\text{Fe}^{3+}$  charge state in DFT, in agreement with the experimental observations.<sup>27</sup> Foreign metal atoms deposited onto this surface adsorb in an oxygen-bridging site in one specific location of the unit cell.<sup>39,41–43</sup> The force-relaxed structure of a Co adatom ( $\text{Co}^{2+}$ ) in such site is shown in Figure 6(a).

The presence of Fe vacancies offers another possibility for Co atoms: incorporation within the surface. In previous work, it was shown that transition metal cations can enter the subsurface, filling one of the cation vacancies. As illustrated by

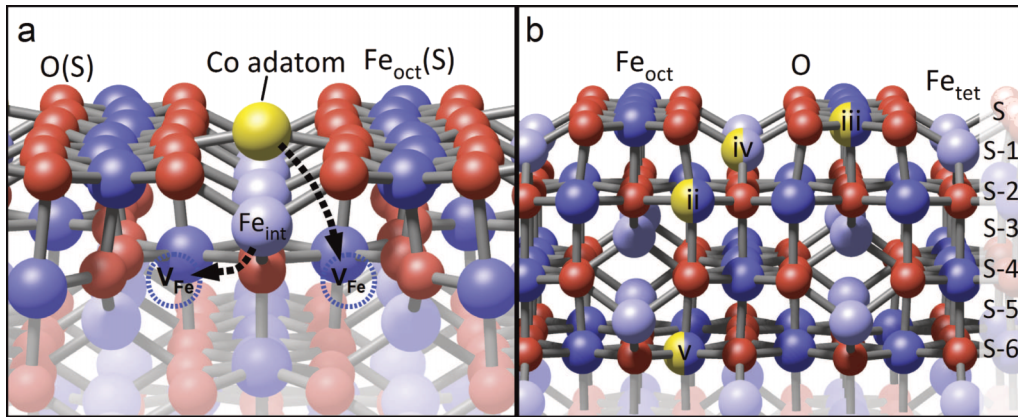


FIG. 6. (a) DFT+U structural model of Co adsorbed at the  $(\sqrt{2} \times \sqrt{2})R45^\circ$ -reconstructed  $\text{Fe}_3\text{O}_4(001)$  surface. The bulk structure is based on an fcc oxygen (red) lattice with Fe cations in octahedral (blue) and tetrahedral (light blue) coordination. The surface reconstruction consists of an ordered array of Fe vacancies and interstitials in the sites indicated in the structure: two octahedral Fe vacancies ( $V_{\text{Fe}}$ , dashed blue circles) and one interstitial tetrahedral iron atom ( $\text{Fe}_{\text{int}}$ ) per reconstructed unit cell introduce the  $(\sqrt{2} \times \sqrt{2})R45^\circ$  periodicity to the surface. The Co adatom (yellow) occupies an oxygen-bridging site between rows of octahedral Fe. The dashed black arrows indicate one possible pathway of Co incorporation: one  $V_{\text{Fe}}$  is filled by  $\text{Fe}_{\text{int}}$  and one by the Co adatom, restoring the number of cations in a bulk-truncated surface. (b) Structural model illustrating the four calculated incorporation sites of Co atoms (atoms with one yellow hemisphere, labeled (ii)-(v)). For all four configurations, the Fe vacancies are filled and the stoichiometry corresponds to a bulk-terminated surface with one Fe atom substituted by one Co atom. The labels (S to S-6) at the right side correspond to the surface (S) and subsurface (S-n) layers.

the dashed arrows in Figure 6(a), this process is accompanied by diffusion of the  $\text{Fe}_{\text{int}}$  atom into the second vacancy,<sup>39</sup> and the spinel cation distribution is locally recovered.

Five different configurations were considered: the Co adatom on the reconstruction (i) and four different sites of incorporated Co (ii)-(v), shown in Figure 6(b) (where also the substrate layer labels are indicated). All five arrangements have the same stoichiometry, so the total energies are directly comparable and can be used to determine the site preference of the incorporated Co atom. Co was considered to occupy either a subsurface octahedral site in the (S-2)-layer (ii), a surface octahedral site (iii), a subsurface tetrahedral site in the (S-1)-layer (iv), or an octahedral site in the bulk-like (S-6) layer (v). In configuration (ii), the vacancies are filled by the interstitial Fe atom ( $\text{Fe}_{\text{int}}$ ) and the deposited Co atom; in all other cases, two Fe atoms fill the vacancies:  $\text{Fe}_{\text{int}}$  and the Fe cation displaced by Co. Since all incorporation pathways require the diffusion of two cations, we assume the barriers involved to be similar (with the exception of configuration (v)). Under this assumption, the total energies can be compared in order to obtain the site preference. The incorporation into deeper layers obviously requires more significant rearrangement and is not facilitated by the presence of the cation vacancies near the surface. Configuration (v) was merely calculated in order to determine whether there is an energetic preference for occupation of bulk layers that would ultimately drive diffusion.

The calculated energies, oxidation states, and magnetic moments for the different configurations of Co at the  $\text{Fe}_3\text{O}_4(001)$  surface are summarized in Table I. The comparison of energies shows that the most favorable incorporation geometry for Co atoms in the surface region is the subsurface octahedral site, in line with results obtained for other 3d transition metals.<sup>39</sup> Furthermore, occupation of octahedral sites in deeper layers is energetically favorable over all. However, while Fe vacancies in the (S-2) layer facilitate incorporation in the surface region, the energy barrier for

diffusion to deeper layers (without vacancies) is expected to be significantly higher. As an estimate, we use the barrier value of  $^{59}\text{Fe}$  in  $\text{Fe}_3\text{O}_4$  (140 kJ/mol), determined by diffusion experiments.<sup>44</sup> Assuming Arrhenius kinetics with a prefactor of  $10^{13} \text{ s}^{-1}$ , significant surface-bulk diffusion (1 hop/s) should begin close to 500 K.<sup>39,44</sup>

The reconstructed  $\text{Fe}_3\text{O}_4(001)$  surface is Fe deficient, and all Fe atoms in the outermost six layers (down to (S-5)) are in a 3+ charge state (and high-spin state). Introducing Co to the system donates charge to the slab. The Co adatom is in a 2+ charge state (the partial charges inside the atomic spheres and in particular the magnetic moments indicate a  $4s^0 3d^7$  state). Like Fe atoms in tetrahedral coordination, Co adatoms couple antiferromagnetically to the surface octahedral Fe cations. The properties of the Fe atoms in the outermost layers remain almost unchanged by the adsorption of Co, but two electrons are transferred to Fe atoms in the (S-4)-layer, which change to  $\text{Fe}^{2+}$ , leading to a small reduction of the Fe total magnetic moment. The calculations of incorporated Co all yield similar results: Co assumes a 2+ charge state, donating charge to the slab, which is transferred to Fe in subsurface layers, resulting in a small increase in  $\text{Fe}^{2+}$ . The exchange coupling of the Co atoms corresponds to the coupling of Fe atoms in equivalent sites: Co in octahedral sites ( $\text{Co}_{\text{oct}}$ ) couples ferromagnetically to octahedral Fe, Co in tetrahedral sites

TABLE I. Calculated energies, oxidation states, and magnetic moments for the five studied different configurations of Co at the  $\text{Fe}_3\text{O}_4(001)$  surface.

Configuration	Energy	Oxidation state	Magnetic moment (in atomic sphere)
Co adatom	-5.46 eV	$\text{Co}^{2+}$	-2.20 $\mu_B$
$\text{Co}_{\text{oct}}(\text{S})$	-5.41 eV	$\text{Co}^{2+}$	+2.62 $\mu_B$
$\text{Co}_{\text{tet}}(\text{S-1})$	-5.27 eV	$\text{Co}^{2+}$	-2.54 $\mu_B$
$\text{Co}_{\text{oct}}(\text{S-2})$	-5.59 eV	$\text{Co}^{2+}$	+2.63 $\mu_B$
$\text{Co}_{\text{oct}}(\text{S-6})$	-5.75 eV	$\text{Co}^{2+}$	+2.60 $\mu_B$



(Co<sub>tet</sub>) antiferromagnetically. The magnetic moments inside the atomic spheres of Co (see Table I) depend weakly on the size of the atomic sphere, but covalency with neighboring O atoms leads to moments slightly smaller than the full Co spin magnetic moment ( $3 \mu_B$ ). The Co adatom exhibits a reduced spin magnetic moment ( $-2.20 \mu_B$ ) mainly owing to weaker spin-polarization of the electrons and a significant amount ( $0.2 e^-$ ) of additional charge in the 3d orbital.

## V. DISCUSSION

The magnetic properties of Fe–Co spinels are complicated by the multiple combinations of possible oxidation states and environment. Ideally, CoFe<sub>2</sub>O<sub>4</sub> has only Co<sup>2+</sup> and Fe<sup>3+</sup> cations. But even in this case, the inversion level can depend on the sample history. While Co is mostly in the octahedral positions, several studies have indicated that up to 30% of the Co population can be in the tetrahedral ones,<sup>2,38</sup> strongly modifying the average magnetic moment. Fe<sup>3+</sup> is in a high-spin state in both tetrahedral and octahedral environments, with a formal spin-moment of  $5 \mu_B$  and a negligible orbital moment in an octahedral environment. Co<sup>2+</sup> is expected to be also in a high-spin configuration with a spin moment of  $3 \mu_B$  and a significant orbital moment. Moving towards iron-rich spinels, iron is found in a Fe<sup>2+</sup> high-spin state, with a formal  $4 \mu_B$  spin moment. Instead, going towards cobalt rich spinels Co<sup>3+</sup>, cations are expected with a low-spin configuration, and thus negligible spin component.

Compared with the bulk, the surface environment offers additional sites for Co incorporation. Among them, based on reported work<sup>39,41–43</sup> and our DFT calculations, we have considered the adatom site on top of two surface oxygen cations in a bridge configuration, the surface octahedral positions, and the subsurface octahedral positions. The latter, as described in the Sec. IV B, corresponds to the lowest total energy position of any Co site, followed by the adatom site and the surface octahedral positions. Although the occupation of deeper layers is energetically favored, the diffusion barrier is expected to be significantly higher, and we thus expect the subsurface site to fill first, followed by a combination of surface octahedral and adatom sites. Indeed, the first step in this sequence has been observed by scanning tunneling microscopy:<sup>39</sup> deposition of 1–2 at/u.c. removes the reconstruction, leaving a partial coverage of Co adatoms.

Our experiments show that the Co magnetic moment depends on the Co dose and annealing temperature. Based on our measurements and the guidance of the DFT calculations, we suggest the following sequence of events in order to explain our data: the first Co at/u.c. deposited at room temperature is incorporated into one of the octahedral vacancies of the  $(\sqrt{2} \times \sqrt{2})R45^\circ$ -reconstructed Fe<sub>3</sub>O<sub>4</sub>(001) surface. Incorporation of the Co atom de-stabilizes the reconstruction, inducing the Fe<sub>int</sub> atom to diffuse into the other remaining vacancy. We emphasize that the presence of vacancies in near-surface region of the reconstructed surface is the reason for the facile incorporation. The end result is a bulk terminated magnetite surface with a Co atom incorporated into an octahedral position. Co in such position has a calculated spin moment of  $+2.63 \mu_B$ , where, as in the

experimental results, a plus sign indicates the same magnetic moment orientation as the Fe octahedral sublattice. Such Co is in a Co<sup>2+</sup> oxidation state, as confirmed by XAS. Once the reconstruction is lifted and in the absence of Fe cation diffusion, only adatom positions are available. Co in such position has the same 2+ oxidation state and a reduced spin moment when compared to the sub-surface octahedral site. But in the adatom position, the spin is oriented in the opposite direction, i.e., antiferromagnetically coupled to the octahedral Fe cations. Experimentally, we observe that after the addition of a total of 6 Co at/u.c., the net Co spin magnetic moment is opposite to the Fe<sub>oct</sub>. Thus, in addition to the sub-surface Co octahedral cation, the remaining cobalt atoms are incorporated into adatom locations. Given the total spin moment of  $-0.8 \mu_B$ , more atoms have to be in the adatom position than in subsurface octahedral ones, as expected due to the limitation of one easy accessible octahedral position per unit cell (characteristic of the vacancies present in the reconstructed surface).

At higher temperatures, cation diffusion is activated<sup>44</sup> and the cobalt atoms can be incorporated deeper into the magnetite crystal. According to the literature, Co atoms are expected to mainly occupy octahedral positions as Co<sup>2+</sup> cations. This would imply a spin magnetic moment aligned with the Fe<sub>oct</sub> one and with a magnitude of  $2.6 \mu_B$  according to the DFT calculations. While the sign is in agreement with the experimental data, the measured magnitude is much smaller,  $0.8 \mu_B$ . Such a reduced value is however in good agreement with those measured in CoFe<sub>2</sub>O<sub>4</sub> thin films.<sup>38</sup> In such case, the difference to the single atom value was attributed to a significant Co population in tetrahedral positions. We lack a direct estimate of the inversion level, but it might be the origin of our reduced moment as well.

For a higher dose of 25 Co at/u.c., the total spin moment per Co<sup>2+</sup> cation just after room temperature deposition is  $+0.5 \mu_B$ , with the same orientation as Fe<sub>oct</sub>. In this case, in addition to oxidized Co atoms, we also observe a metallic Co peak by XPS. The surface lattice constant of the resulting surface is half the magnetite one, as evidenced by the disappearance of the first order spots and the presence of the second order ones in the LEED pattern. This could be due to some ordering of the deposited Co, or, alternatively, it could be ascribed to a partially disordered magnetite surface where the difference between each magnetite subunit is lost. Further work will be needed to determine this detail. Regarding the magnetic properties of the Co atoms and given the positive value of the average magnetic moment, we assume that the exchange coupling to magnetite is ferromagnetic, with the metallic contribution driving the averaged Co spin magnetic moment to positive values (metallic Co is expected to have a magnetic moment per atom of  $1.6 \mu_B$ <sup>32</sup>). After the first annealing step, all metallic Co disappears, and the average Co magnetic moment changes sign to  $-0.4 \mu_B$ . This suggests that we are now in a situation similar to the low coverage experiment before annealing, with more atoms located in adatom positions instead of subsurface ones and none with metallic character. Further annealing gives rise to Co incorporation into the crystal occupying preferentially octahedral positions as Co<sup>2+</sup>, aligning the magnetic moment



again with the Fe<sub>oct</sub> and changing the sign of the Co magnetic moment to positive, as shown in Figure 4. XMCD indicates that when driven deeper into the crystal, Co populates mostly the octahedral sites.

At higher temperatures, the average magnetic moment increases with annealing temperature, and the Co concentration decreases as Co is incorporated deeper into the magnetite crystal. A possible reason for this evolution is the presence of a Co-rich layer after the 658 K annealing stage. If the Co:Fe ratio locally exceeds 1:2, we would expect to have some Co<sup>3+</sup> atoms, which given their low-spin configuration would not contribute to the spin moment, giving rise to a low averaged Co magnetic moment. Indeed, the XPS spectrum suggests the presence of some Co<sup>3+</sup>. Further annealing would dilute such Co-rich region, removing any Co<sup>3+</sup>, and bringing back Co<sup>2+</sup> with an intermediate inversion level and increasing the averaged magnetic moment per Co atom, as experimentally observed. To ascertain the presence and role of a small amount of Co<sup>3+</sup>, further work will be needed.

## VI. CONCLUSIONS

We have studied the incorporation of Co atoms on a magnetite single crystal with (001) orientation by a combination of XPS and LEED and spatially resolved XAS and XMCD at the Fe and Co L edges, an approach which permits addressing the structure, oxidation state, magnetic domain pattern, and magnitude of the cationic magnetic moments.

At all times, the magnetic domain distribution observed at the Co atoms exactly matches the one from the Fe cations. Initially, Co goes into a sub-surface octahedral position, removing the surface reconstruction. Additional atoms are located as adatoms on the surface, giving an average Co magnetic moment aligned opposite to the Fe octahedral one. Annealing causes Co atoms to incorporate into deeper crystal positions, mostly into octahedral ones with a significant inversion level as detected by magnitude and sense of the Co magnetic moment.

The fact that the intimate relation between chemical environment and magnetic moment is established has relevant consequences for both the characterization and the tunability of the spinel properties. On one hand, we demonstrate that evaluation of the magnetic moment permits an accurate determination of the chemical environment of the cation being incorporated into the lattice. On the other hand, careful annealing schedules can be designed in order to select a desired cationic location and in consequence to tune the magnetic properties. Our approach can be used for studying the incorporation of other magnetic atoms on magnetite or more generally on any magnetic spinel.

## ACKNOWLEDGMENTS

This research was supported by the Spanish Ministry of Economy and Competitiveness (MINECO) through Project Nos. MAT2012-38045-C04-01, MAT2013-48009-C4-1-P, MAT2015-64110-C2-1-P and MAT2015-64110-C2-2-P and by the European Union 7th framework programme NANOPYME Project (No. 310516). These experiments were performed at the CIRCE beamline of the ALBA Synchrotron

Light Facility with the collaboration of ALBA staff. We thank A.K. Schmid for his help with and loan of the magnetite crystal. G.S.P. and R.B. acknowledge funding from the Austrian Science Fund START Prize Y 847-N20 and Project No. P24925-N20. R.B. acknowledges a stipend from the Vienna University of Technology. Both R.B. and P.B. acknowledge support from the Austrian Science Fund doctoral college SOLIDS4FUN, project number W1243, while L.M.-G. does from an FPI contract with Reference No. BES-2013-063396 from the MINECO. Part of the DFT calculations were performed at the Vienna Scientific Cluster.

- <sup>1</sup>X. Zhang, V. Stevanović, M. d'Avezac, S. Lany, and A. Zunger, "Prediction of A<sub>2</sub>BX<sub>4</sub> metal-chalcogenide compounds via first-principles thermodynamics," *Phys. Rev. B* **86**, 014109 (2012).
- <sup>2</sup>M. Takahashi and M. E. Fine, "Magnetic behavior of quenched and aged CoFe<sub>2</sub>O<sub>4</sub>-Co<sub>3</sub>O<sub>4</sub> alloys," *J. Appl. Phys.* **43**, 4205-4216 (1972).
- <sup>3</sup>J. A. Moyer, C. A. F. Vaz, E. Negusse, D. A. Arena, and V. E. Henrich, "Controlling the electronic structure of Co<sub>1-x</sub>Fe<sub>2+x</sub>O<sub>4</sub> thin films through iron doping," *Phys. Rev. B* **83**, 035121 (2011).
- <sup>4</sup>F. Y. Ran, Y. Tsunemaru, T. Hasegawa, Y. Takeichi, A. Harasawa, K. Yaji, S. Kim, and A. Kakizaki, "Valence band structure and magnetic properties of Co-doped Fe<sub>3</sub>O<sub>4</sub>(100) films," *J. Appl. Phys.* **109**, 123919 (2011).
- <sup>5</sup>R. M. Cornell and U. Schwertmann, *The Iron Oxides* (John Wiley & Sons Ltd, Weinheim, 1997).
- <sup>6</sup>W. L. Roth, "The magnetic structure of Co<sub>3</sub>O<sub>4</sub>," *J. Phys. Chem. Solids* **25**, 1-10 (1964).
- <sup>7</sup>*Handbook of Magnetism and Advanced Magnetic Materials*, 5th ed., edited by H. Kronmüller and S. Parkin (Wiley-Blackwell, 2007).
- <sup>8</sup>A. Lopez-Ortega, E. Lottini, C. de Julián Fernández, and C. Sangregorio, "Exploring the magnetic properties of cobalt-ferrite nanoparticles for the development of a rare-earth-free permanent magnet," *Chem. Mater.* **27**, 4048 (2015).
- <sup>9</sup>P. J. van der Zaag, P. J. H. Bloemen, J. M. Gaines, R. M. Wolf, P. A. A. van der Heijden, R. J. M. van de Veerdonk, and W. J. M. de Jonge, "On the construction of an Fe<sub>3</sub>O<sub>4</sub>-based all-oxide spin valve," *J. Magn. Magn. Mater.* **211**, 301-308 (2000).
- <sup>10</sup>F. Rigato, S. Piano, M. Foerster, F. Giubileo, A. M. Cucolo, and J. Fontcuberta, "Andreev reflection in ferrimagnetic CoFe<sub>2</sub>O<sub>4</sub> spin filters," *Phys. Rev. B* **81**, 174415 (2010).
- <sup>11</sup>M. Bibes, J. E. Villegas, and A. Barthélémy, "Ultrathin oxide films and interfaces for electronics and spintronics," *Adv. Phys.* **60**, 5-84 (2011).
- <sup>12</sup>P. Seneor, A. Fert, J.-L. Maurice, F. Montaigne, F. Petroff, and A. Vaurès, "Large magnetoresistance in tunnel junctions with an iron oxide electrode," *App. Phys. Lett.* **74**, 4017 (1999).
- <sup>13</sup>E. Wada, K. Watanabe, Y. Shirahata, M. Itoh, M. Yamaguchi, and T. Taniyama, "Efficient spin injection into GaAs quantum well across Fe<sub>3</sub>O<sub>4</sub> spin filter," *Appl. Phys. Lett.* **96**, 102510 (2010).
- <sup>14</sup>D. G. Rethwisch and J. A. Dumesic, "The effect of metal-oxygen bond strength on properties of oxides. II. Water-gas shift over bulk oxides," *Appl. Catal.* **21**, 97 (1986).
- <sup>15</sup>C. Ratnasamy and J. P. Wagner, "Water gas shift catalysis," *Catal. Rev.-Sci. Eng.* **51**, 325 (2009).
- <sup>16</sup>G. S. Parkinson, Z. Novotny, P. Jacobson, M. Schmid, and U. Diebold, "Room temperature water splitting at the surface of magnetite," *J. Am. Chem. Soc.* **133**, 12650 (2011).
- <sup>17</sup>G. A. Huff and C. N. Satterfield, "Intrinsic kinetics of the Fischer-Tropsch synthesis on a reduced fused-magnetite catalyst," *Ind. Eng. Chem. Process Des. Dev.* **23**, 696 (1984).
- <sup>18</sup>J. A. Koza, Z. He, A. S. Miller, and J. A. Switzer, "Electrodeposition of crystalline Co<sub>3</sub>O<sub>4</sub>-a catalyst for the oxygen evolution reaction," *Chem. Mater.* **24**, 3567 (2012).
- <sup>19</sup>K. R. Rao, P. K. Rao, S. Masthan, L. Kaluschnaya, and V. Shur, "New type of carbon coated alumina supports for the preparation of highly active ruthenium catalysts for ammonia synthesis," *App. Catal.* **62**, L19 (1990).
- <sup>20</sup>G. Zhao, Z. Xu, and K. Sun, "Hierarchical porous Co<sub>3</sub>O<sub>4</sub> films as cathode catalysts of rechargeable Li-O<sub>2</sub> batteries," *J. Mater. Chem. A* **1**, 12862 (2013).
- <sup>21</sup>P. Lavela, G. F. Ortiz, J. L. Tirado, E. Zhecheva, R. Stoyanova, and S. Ivanova, "High-performance transition metal mixed oxides in conversion electrodes: A combined spectroscopic and electrochemical study," *J. Phys. Chem. C* **111**, 14238-14246 (2007).

- <sup>22</sup>A. K. Rai, J. Gim, T. V. Thi, D. Ahn, S. J. Cho, and J. Kim, "High rate capability and long cycle stability of  $\text{Co}_3\text{O}_4/\text{CoFe}_2\text{O}_4$  nanocomposite as an anode material for high-performance secondary lithium ion batteries," *J. Phys. Chem. C* **118**, 11234–11243 (2014).
- <sup>23</sup>J. R. Goldstein and A. C. C. Tseung, "The kinetics of hydrogen peroxide decomposition catalyzed by cobalt-iron oxides," *J. Catal.* **32**, 452–465 (1974).
- <sup>24</sup>N. Bahlawane, P. H. T. Ngamou, V. Vannier, T. Kottke, J. Heberle, and K. Kohse-Höinghaus, "Tailoring the properties and the reactivity of the spinel cobalt oxide," *Phys. Chem. Chem. Phys.* **11**, 9224 (2009).
- <sup>25</sup>L. Martín-García, A. Quesada, C. Munuera, J. F. Fernández, M. García-Hernández, M. Foerster, L. Aballe, and J. de la Figuera, "Atomically flat ultrathin cobalt ferrite islands," *Adv. Mater.* **27**, 5955–5960 (2015).
- <sup>26</sup>J. B. Moussy, "From epitaxial growth of ferrite thin films to spin-polarized tunnelling," *J. Phys. D: Appl. Phys.* **46**, 143001 (2013).
- <sup>27</sup>R. Bliem, E. McDermott, P. Ferstl, M. Setvin, O. Gamba, M. Schneider, M. Schmid, U. Diebold, P. Blaha, L. Hammer, and G. Parkinson, "Surface cation vacancy stabilization of the magnetite (001) surface," *Science* **346**, 1215–1218 (2014).
- <sup>28</sup>L. Aballe, M. Foerster, E. Pellegrin, J. Nicolas, and S. Ferrer, "The ALBA spectroscopic LEEM-PEEM experimental station: Layout and performance," *J. Synchrotron Radiat.* **22**, 745–752 (2015).
- <sup>29</sup>K. F. McCarty and J. de la Figuera, "Low-energy electron microscopy," in *Surface Science Techniques*, Springer Series in Surface Sciences (Springer, Berlin, Heidelberg, 2013), Vol. 51, p. 531.
- <sup>30</sup>W. Kuch and C. M. Schneider, "Magnetic dichroism in valence band photoemission," *Rep. Prog. Phys.* **64**, 147–204 (2001).
- <sup>31</sup>M. Monti, B. Santos, A. Mascaraque, O. Rodríguez de la Fuente, M. A. Niño, T. O. Montes, A. Locatelli, K. F. McCarty, J. F. Marco, and J. de la Figuera, "Magnetism in nanometer-thick magnetite," *Phys. Rev. B* **85**, 020404 (2012).
- <sup>32</sup>C. T. Chen, Y. U. Idzerda, H.-J. Lin, N. V. Smith, G. Meigs, E. Chaban, G. H. Ho, E. Pellegrin, and F. Sette, "Experimental confirmation of the x-ray magnetic circular dichroism sum rules for iron and cobalt," *Phys. Rev. Lett.* **75**, 152–155 (1995).
- <sup>33</sup>P. Blaha, K. Schwarz, G. K. H. Madsen, D. Kvasnicka, and J. Luitz, *WIEN2K, An Augmented Plane Wave+Local Orbitals Program for Calculating Crystal Properties* (Karlheinz Schwarz, Technical Universität Wien, Austria, 2001).
- <sup>34</sup>J. P. Perdew, K. Burke, and M. Ernzerhof, "Generalized gradient approximation made simple," *Phys. Rev. Lett.* **77**, 3865–3868 (1996).
- <sup>35</sup>J. de la Figuera, L. Vergara, A. T. N'Diaye, A. Quesada, and A. K. Schmid, "Micromagnetism in (001) magnetite by spin-polarized low-energy electron microscopy," *Ultramicroscopy* **130**, 77 (2013).
- <sup>36</sup>L. Martín-García, R. Gargallo-Caballero, M. Monti, M. Foerster, J. F. Marco, L. Aballe, and J. de la Figuera, "Spin and orbital magnetic moment of reconstructed  $\sqrt{2} \times \sqrt{2} \text{R}45^\circ$  magnetite (001)," *Phys. Rev. B* **91**, 020408 (2015).
- <sup>37</sup>E. Pellegrin, M. Hagelstein, S. Doyle, H. Moser, J. Fuchs, D. Vollath, S. Schuppler, M. James, S. Saxena, L. Niesen, O. Rogojanu, G. Sawatzky, C. Ferrero, M. Borowski, O. Tjernberg, and N. Brookes, "Characterization of nanocrystalline  $\gamma\text{-Fe}_2\text{O}_3$  with synchrotron radiation techniques," *Phys. Status Solidi B* **215**, 797–801 (1999).
- <sup>38</sup>J. A. Moyer, C. A. F. Vaz, D. A. Arena, D. Kumah, E. Negusse, and V. E. Henrich, "Magnetic structure of Fe-doped  $\text{CoFe}_2\text{O}_4$  probed by x-ray magnetic spectroscopies," *Phys. Rev. B* **84**, 054447 (2011).
- <sup>39</sup>R. Bliem, J. Pavelec, O. Gamba, E. McDermott, Z. Wang, S. Gerhold, M. Wagner, J. Osiecki, K. Schulte, M. Schmid, P. Blaha, U. Diebold, and G. Parkinson, "Adsorption and incorporation of transition metals at the magnetite  $\text{Fe}_3\text{O}_4(001)$  surface," *Phys. Rev. B* **92**, 075440 (2015).
- <sup>40</sup>G. F. M. Gomes, T. E. P. Bueno, D. E. Parreiras, G. J. P. Abreu, A. de Siervo, J. C. Cezar, H.-D. Pfannes, and R. Paniago, "Magnetic moment of  $\text{Fe}_3\text{O}_4$  films with thicknesses near the unit-cell size," *Phys. Rev. B* **90**, 134422 (2014).
- <sup>41</sup>Z. Novotný, G. Argentero, Z. Wang, M. Schmid, U. Diebold, and G. S. Parkinson, "Ordered array of single adatoms with remarkable thermal stability:  $\text{Au}/\text{Fe}_3\text{O}_4(001)$ ," *Phys. Rev. Lett.* **108**, 216103 (2012).
- <sup>42</sup>G. S. Parkinson, Z. Novotny, G. Argentero, M. Schmid, J. Pavelec, R. Kosak, P. Blaha, and U. Diebold, "Carbon monoxide-induced adatom sintering in a  $\text{Pd-Fe}_3\text{O}_4$  model catalyst," *Nat. Mater.* **12**, 724–728 (2013).
- <sup>43</sup>R. Bliem, R. Kosak, L. Perneczky, Z. Novotny, O. Gamba, D. Fobes, Z. Mao, M. Schmid, P. Blaha, U. Diebold, and G. S. Parkinson, "Cluster nucleation and growth from a highly supersaturated adatom phase: Silver on magnetite," *ACS Nano* **8**, 7531–7537 (2014).
- <sup>44</sup>R. Dieckmann and H. Schmalzried, "Defects and cation diffusion in magnetite (II)," *Ber. Bun. Phys. Chem.* **81**, 414–419 (1977).